The Astrophysical Journal, 759:38 (10pp), 2012 November 1 doi:10.1088/0004-637X/759/1/38

A THEORETICAL COLOR–VELOCITY CORRELATION FOR SUPERNOVAE ASSOCIATED WITH GAMMA-RAY BURSTS

Sharon Rapoport[1,2], Stuart A. Sim[1,2], Keiichi Maeda[3], Masaomi Tanaka[4], Markus Kromer[5], Brian P. Schmidt[1,2], and Ken'ichi Nomoto[3]
[1] Research School of Astronomy and Astrophysics, The Australian National University, Weston Creek, ACT 2611, Australia
[2] ARC Centre of Excellence for All-sky Astrophysics (CAASTRO)
[3] The Institute of Physics and Mathematics of the Universe, University of Tokyo, Tokyo, Japan
[4] National Astronomical Observatory, Mitaka, Tokyo, Japan
[5] Max Plank Institute for Astrophysics, Garching, Germany
Received 2012 June 20; accepted 2012 September 20; published 2012 October 15

ABSTRACT

We carry out the first multi-dimensional radiative transfer calculations to simultaneously compute synthetic spectra and light curves for models of supernovae driven by fast bipolar outflows. These allow us to make self-consistent predictions for the orientation dependence of both color evolution and spectral features. We compare models with different degrees of asphericity and metallicity and find significant observable consequences of both. In aspherical models, we find spectral and light curve features that vary systematically with observer orientation. In particular, we find that the early-phase light curves are brighter and bluer when viewed close to the polar axis but that the peak flux is highest for equatorial (off-axis) inclinations. Spectral line features also depend systematically on observer orientation, including the velocity of the Si II 6355 Å line. Consequently, our models predict a correlation between line velocity and color that could assist the identification of supernovae associated with off-axis jet-driven explosions. The amplitude and range of this correlation depends on the degree of asphericity, the metallicity, and the epoch of observation but we find that it is always present and acts in the same direction.

Key words: gamma-ray burst: general – radiative transfer – supernovae: general

Online-only material: color figures

1. INTRODUCTION

Gamma-ray bursts (GRBs) provide a powerful tool to study galaxy formation at high redshifts (e.g., Conselice et al. 2005) and provide a unique opportunity to observe extreme physical processes (e.g., Bucciantini et al. 2009; Woosley & Heger 2006). Long-duration GRBs (LGRBs) have been shown to be connected with broad-lined Type Ic supernovae (SNe Ic; Galama et al. 1998; Iwamoto et al. 1998; Kulkarni et al. 1998; Bloom et al. 1999; Mészáros 2006; Lindner et al. 2010), implying that they are linked to the collapse of a massive star; see Woosley & Bloom (2006) for a review. However, the exact nature of this connection is not yet understood, and is especially poorly constrained in the very bright GRBs used to study the high-redshift universe.

The collapsar model (Woosley 1993; MacFadyen & Woosley 1999) predicts that when the iron core of a massive rotating star collapses into a black hole (BH), material accretes onto the BH via a rotating disk. A narrow, highly relativistic jet is launched at the BH–accretion-disk boundary which gives rise to the observed GRB. In addition, a sub-relativistic wind is driven off the disk, which drives the explosion of the star. Nucleosynthesis in the explosion produces ^{56}Ni, the decay of which powers the SN emission (Iwamoto et al. 1998). Angular momentum is believed to be a crucial factor in determining the mass that collapses into the BH. A more massive BH implies lower density in the accretion disk, which might disfavor production of a GRB (Woosley & Zhang 2007). As higher metallicity leads to greater mass loss via stellar winds, which causes the star to lose angular momentum, GRB progenitors are expected to have low metallicity (Heger et al. 2003; Yoon & Langer 2005). In the close binary progenitor scenario, the metallicity dependence is much weaker (e.g., Fryer et al. 2007).

Observationally, this collapsar model implies that emission produced in the highly collimated jet is strongly affected by relativistic beaming such that it is only detectable when the Earth is closely aligned with the jet direction. Therefore, detection of a GRB immediately suggests that the event is observed pole-on (along the rotation axis). In contrast, the associated SN could be observed from all orientations, although its properties can be expected to depend on viewing angle.

Studying the SN associated with LGRBs is one means to better understand the explosion mechanism. Analysis of SN 1998bw, the first SN believed to host an LGRB, supports the high-mass collapsar model (Iwamoto et al. 1998; Woosley et al. 1999; MacFadyen & Woosley 1999) and gives an estimated main-sequence progenitor mass of ∼30–40 $M_{\odot}$. However, this object's γ-ray luminosities were orders of magnitude lower than the typical GRBs studied at high redshifts and it is thus not typical of the class. Subsequent modeling of a variety of SNe associated with GRBs has revealed a wide distribution in the kinetic energy (E_k), ejecta mass ($M_{\rm ej}$), and ^{56}Ni mass (M_{56}) parameter space (e.g., Nomoto et al. 2004, 2006). For example, in 2003, SN2003dh/GRB 030329 became the first bright GRB to have its SN studied in detail (Hjorth et al. 2003; Stanek et al. 2003). At redshift $z = 0.169$ (Greiner et al. 2003), it was the first nearby GRB associated with an SN to have γ-ray and afterglow properties similar to those observed for cosmological GRBs (Price et al. 2003). Also, Berger et al. (2011) recently observed the cosmological GRB/SN 2009nz, and reported broad line features with lower velocities than 1998bw. However, as explosion parameters are often estimated using the simple Arnett relation (Arnett 1982), more detailed modeling is warranted (see Section 4).

The collapsar scenario for LGRB–SN predicts that in many cases we will be able to observe the SN explosion but will not

see the GRB because of our orientation. One way to test the model is to hunt for the predicted population of asymmetric SN explosions in which our line of sight is off the jet axis. A promising approach is radio surveys looking for emission associated with the interaction of relativistic outflow with a previously emitted wind or the circumstellar material. Based on a sample of 68 Ib/c SNe, Soderberg et al. (2006) argued that $\lesssim$10% of Type Ib/c SNe are associated with off-axis jets. However, radio observations have also shown that outflows powered by a central engine may be present in some objects for which no GRB was detected (Soderberg et al. 2010).

Other phenomena that could be explained as an off-axis GRB include X-ray flashes (Yamazaki et al. 2004), which were also found to sometimes be associated with SNe (e.g., XRF100316D/SN2010bh; Olivares E. et al. 2012; Bufano et al. 2012; Cano et al. 2011, XRF060218/SN2006aj; Campana et al. 2006; Pian et al. 2006). Some evidence for jet-like SN explosions has also been uncovered via late-time optical observations of stripped-envelope core-collapse SNe. Once the ejecta is optically thin, the observed blueshifted and redshifted lines follow the shape of the ejecta. In this stage, double-peaked line profiles arise when a bipolar SN is observed off-axis (Maeda et al. 2002), and some cases were detected and analyzed by, for example, Maeda et al. (2008) and Taubenberger et al. (2009).

The aforementioned studies of radio emission and late-time optical spectra are powerful tools to search for evidence of jets having been involved in SN explosions. However, signatures are also expected in ultraviolet/optical/near-infrared emission around maximum light of the SN explosion. Observations of this phase are typically more complex to interpret than, e.g., late-phase nebular spectra but are extremely important since they are the most routinely accessible data. To interpret such data requires suitable explosion models and synthetic spectra and light curves. The quest to understand the GRB–SN connection has led to the development of numerous hydrodynamical studies of jet-driven models. Proga et al. (2003) and later Sawai et al. (2005) showed via simulations that magnetohydrodynamical processes alone can launch and sustain polar outflows from the accretion disk around a BH formed by the collapse of the core of a massive star. The success of such simulations of jet launching has ignited a study of theoretical modeling of asymmetric SNe. In particular, hydrodynamical simulations of asymmetric explosion models have been conducted (Maeda et al. 2002, 2006; Maeda 2006; Tanaka et al. 2007), and compared with observations, mostly looking for a promising model to explain the extraordinary SN 1998bw.

In this paper, our goal is to carry out self-consistent, multi-dimensional, time-dependent radiative transfer simulations to predict the angle-dependent spectra and light curves for asymmetric SNe Ic. In previous studies (e.g., Tanaka et al. 2007), light curves were calculated with a very simplified treatment of opacity while spectra were computed separately using a time-independent approach. Our new self-consistent calculations will help quantify the observable signatures of a jet-driven explosion and, in particular, allow us to predict the differences in optical colors and spectral features that are expected for a jet-driven explosion viewed off-axis. As input, we work with the asymmetric explosion models of (Maeda et al. 2002, hereafter M02). We also investigate the influence of progenitor metallicity on the optical observables since several studies have suggested a possible link between the metallicity of the SN environment and whether it will produce a GRB (Sollerman et al. 2005; Modjaz et al. 2008, 2006; Levesque et al. 2010). We begin (Section 2) by describing the explosion models and principles of our radiative transfer code. In Section 3 we outline our results and in Section 4 we discuss our conclusions.

Table 1
Explosion Models

Model	$M_{\rm ej}(M_\odot)$	$M_{56}(M_\odot)$	$E_k(E_{51})$	α/β[a]
A1 (A0.1)	10.10	0.23	20	16
C1 (C0.1)	10.05	0.28	20	8
F1 (F0.1)	10.08	0.38	20	1

Note. [a] Asphericity parameter—see the text for details.

2. METHODS

2.1. Explosion Models

For this study, we adopt the jet-driven explosion models of M02. These were created by exploding the core of a star that had initial mass of 40 $M_\odot$ (Iwamoto et al. 1998). A cut in mass coordinate (at 2.4 $M_\odot$) was used to divide the core model into an inner region, which is assumed to collapse to a BH, and an outer region that will form the SN ejecta. Two-dimensional hydrodynamical and nucleosynthesis calculations were performed to simulate the explosion of the outer layers. The explosions were driven by inserting an excess of kinetic energy in the region below the mass cut. This gives rise to a shock which propagates through the model, unbinding the material and triggering nuclear burning. All models have a total ejecta mass of $\sim$10 $M_\odot$, although small deviations arise owing to the treatment of boundary conditions in the hydrodynamic simulations. Different asphericities were induced in the models by varying the injection of the kinetic energy. Specifically, direction-dependent initial velocities were imposed such that the velocity along the polar (i.e., assumed jet) axis ($v_z = \alpha z$) was larger than that along the equatorial direction ($v_r = \beta r$). The degree of asphericity is conveniently parameterized by the ratio α/β.

The M02 models explored a range of values for the final kinetic energy and degree of asphericity. Since this study focuses on the effect of asphericity on the light curves and spectra, we will consider only a subset of their models that have a fixed final kinetic energy of $E_{51} = 20$ ($E_{51} \equiv E_{\rm iso}/10^{51}$ ergs): models A, C, and F of M02. Of these, model A is the most aspherical, C has intermediate sphericity, and model F is spherically symmetric. Important parameters of these models, and their ^{56}Ni yields, are given in Table 1.

Observations of SNe associated with LGRBs do not reveal any H or He. Modeling of SN1998bw was successful when using as a progenitor a core stripped down to its O layer by the time of explosion (Maeda et al. 2002). Therefore, for our radiative transfer calculations the composition of all unburnt material has been set to that of the O layer with a small fraction ($\sim$1%) of C (i.e., we do not include any He-rich material in the ejecta). To explore the effect of progenitor metallicity, we have included all abundances of elements heavier than Na (up to atomic number 30) in the composition of the unburnt material. We adopted the solar elemental abundances of Anders & Grevesse (1989) and have computed synthetic observables for models with metallicities (relative to solar) of $Z = 0.1\ Z_\odot$ and $Z = 1\ Z_\odot$. Note that the solar element abundances have only been added to the input conditions for our radiative transfer simulations—i.e., we explore the effect of metallicity in the

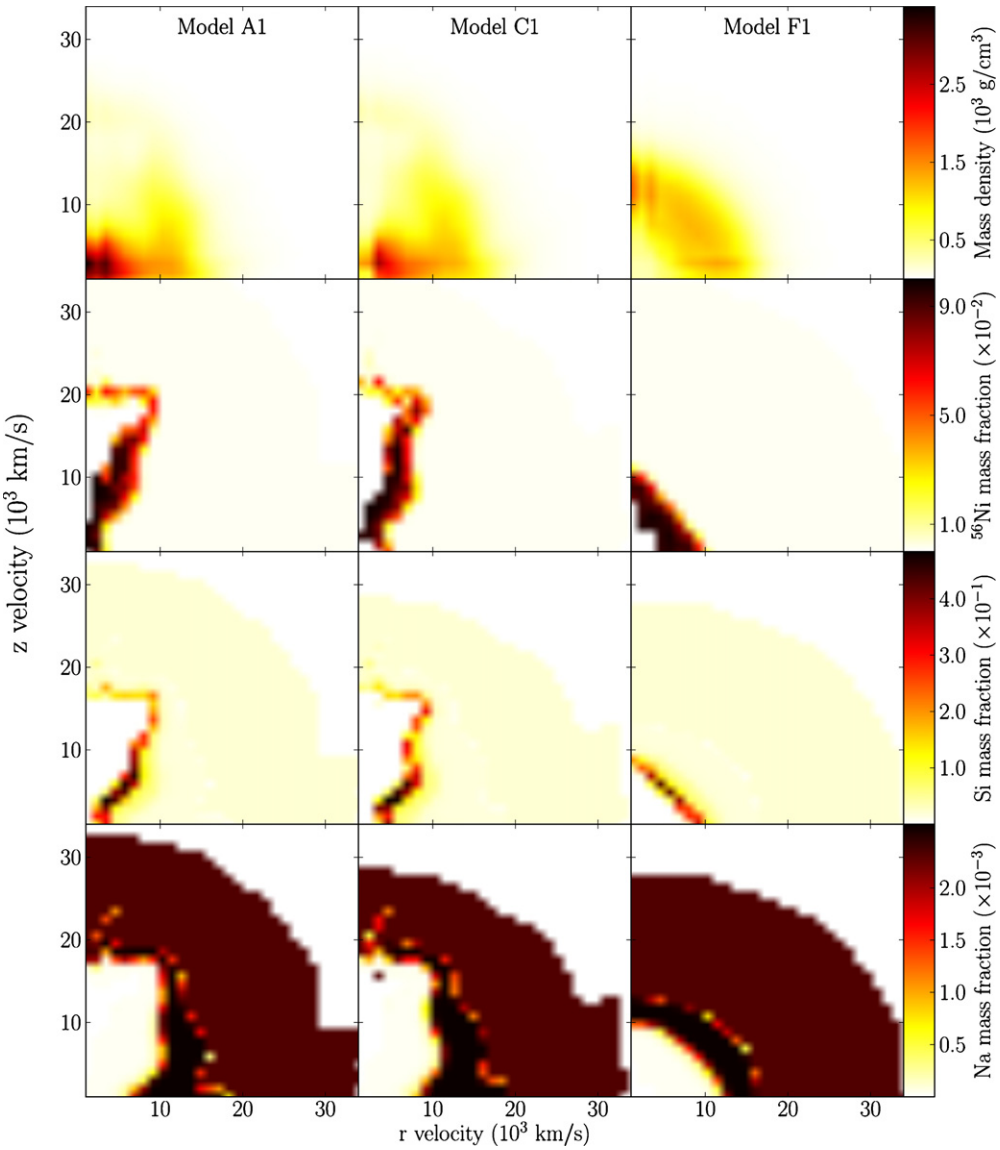

Figure 1. Left column: model A1; middle column: model C1; right column: model F1. From top to bottom: total mass density, ^{56}Ni, Si, and Na mass fractions. While model F is spherically symmetric, the "line" shape seen for the Si and ^{56}Ni mass fractions is due to numeric effect as hydrodynamic simulations tend to give artifacts near the imposed axes of symmetry. The bulging along the equatorial is another simulation feature due to numeric effects and the colliding at the equator of the bow shocks which are driven by the jet.

(A color version of this figure is available in the online journal.)

unburnt material on the synthetic spectra and light curves but do not investigate how progenitor metallicity influences either the hydrodynamics or nucleosynthesis of the burnt material. In addition, the metallicity of the primordial material of a star will influence its evolution (e.g., Meynet et al. 2009). This will affect the abundances and stellar structure at the time of collapse, which will alter the expected SN spectra and light curve. We plan to investigate the expected variations in a forthcoming paper (S. Rapoport et al. 2012, in preparation), in which we consider a wider range of progenitor models. Throughout this paper, we will denote our calculations adopting solar metallicity for the M02 models A (C, F) as A1 (C1, F1) and those for sub-solar metallicity ($Z = 0.1\ Z_{\odot}$) as A0.1 (C0.1, F0.1).

Figure 1 illustrates the spatial distribution of mass density and the abundances for key elements that will feature in our discussion. In the aspherical models (A1, C1), the explosion dynamics gives rise to a relatively dense core region that is extended in the equatorial direction. In contrast, the polar region (i.e., the direction in which the high velocities were initially injected) has relatively low density. ^{56}Ni is produced by explosive Si burning and, in all aspherical models, its mass fraction is highest in the low-density regions. This gives a near-conical shape to the ^{56}Ni distribution for the most aspherical model (see also Figure 2 in Maeda et al. 2006). When the degree of asphericity is reduced (model C1), the ^{56}Ni distribution no longer flares out from the pole and gradually looks more like the spherically symmetric model (F1).

Si (and other intermediate-mass elements) is produced by explosive O burning (e.g., Nomoto et al. 2006). Its abundance distribution is similar in shape to ^{56}Ni, being concentrated around the outer edge of the ^{56}Ni-rich region. Si is also present in small quantities in the outer layers since we have assumed non-zero progenitor metallicities in all models. The Na in our models is dominated by the contribution in the unburnt material.

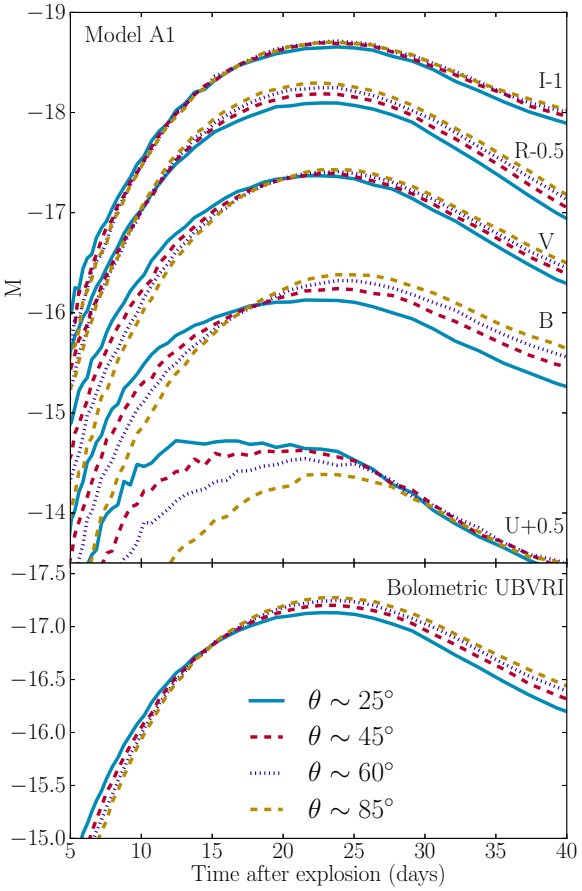

Figure 2. Light curves for model A1 for the different viewing angles. $\theta = 0°$ is the jet direction and $\theta = 90°$ is the equator. See the top panel of Figure 5 for the filter curves.

(A color version of this figure is available in the online journal.)

Its abundance distribution is therefore comparatively uniform and its concentration highest in the outer layers.

2.2. Radiative Transfer

Our radiative transfer simulations were carried out using *ARTIS* (Sim 2007; Kromer & Sim 2009), which is a Monte Carlo (MC), multi-dimensional, time-dependent, radiative transfer code based on the methods described by Lucy (2002, 2003, 2005). The code computes synthetic spectra for SN explosion models assuming homologous expansion of the ejecta and the Sobolev approximation for line opacity. MC radiative transfer methods has been applied to a variety of SN explosion models and tested by comparison to other calculations in, e.g., Kasen et al. (2006) (using the *SEDONA* code) and Kromer & Sim (2009) (for *ARTIS*). Here, for the first time, we apply *ARTIS* to models for SNe Ic. We note that, for SNe Ic explosions with a compact progenitor, homologous expansion is expected to be reached within the first ∼10 s and is therefore a good approximation at the times of ∼days that will be studied here.).

As input, the code requires specification of the velocity, density, and composition for each grid cell (a Cartesian grid is used). The total energy emitted from the decay chain ^{56}Ni→^{56}Co→^{56}Fe is determined from the model and is divided into a set of MC quanta. At the start of the radiative transfer simulation, these quanta are placed in the model according to the ^{56}Ni densities in the form of radioactive pellets (Lucy 2005). During the simulation these convert into photon packets in accordance with the radioactive decay times. The photon packets then propagate through the model of the ejecta and can interact with the medium via Compton scattering, pair production, bound–free and bound–bound absorption. For bound–bound transitions we use a line list extracted from the data of Kurucz & Bell (1995) CD23, as describe in Kromer & Sim (2009). The time, direction, and frequency of escaping energy quanta are recorded to allow angle-dependent spectra and light curves to be created. We refer the reader to Kromer & Sim (2009) for full details on the MC techniques employed by *ARTIS*.

Spectra were generated for models A1, A0.1, C1, C0.1, F1, and F0.1. The simulations were started at three days after explosion and were run until 50 days after explosion with 60 time steps, logarithmically spaced. While a study of the models at earlier start time is appealing, the high opacities immediately after explosion result in a heavy computation requirement. In addition, this paper focuses on SNe associated with real GRBs, where early-time SN properties are practically undetectable under the luminous GRB afterglow—consequently predictions for very early times are not easily testable. A grid of 68 × 68 × 68 cells was used, giving a resolution of ∼1180 km s^{-1}. As the explosion models are two dimensional with symmetry along the jet direction, the synthetic observables depend only on the angle (θ) between the observer line of sight and the polar axis of the model. For the aspherical models, we extracted synthetic observables for five values of θ by dividing the emergent MC quanta into five bins of equal solid angle across the range $0° < \theta < 90°$.

Table 2
V-band Maximum Light Times in Days after Explosion

	V			
Model	25°[a,b]	45°	60°	85°
A1	22	24	24	24
A0.1	20	22	22	22
C1	24	24	24	24
C0.1	23	24	24	24
F1		29		
F0.1		28		

Notes. [a] Values are quoted for four observer inclination angles (measured relative to the polar axis).
[b] One number for all columns implies no angle dependency.

3. RESULTS

3.1. Light Curves

The main advantage of our simulations compared to previous studies of the M02 explosion models (Tanaka et al. 2007, hereafter T07) is a self-consistent, time-dependent treatment of the spectral evolution. This means we can extract light curves that are fully consistent with both the spatial distribution of ^{56}Ni in the model and the detailed opacities needed to compute realistic spectra. Figure 2 shows light curves for the standard Bessell (Bessell & Murphy 2012) *U*, *B*, *V*, *R*, and *I* filters[6] for model A1 for four different observer orientations. We also show the bolometric *U V O I R* light curves, defined by a top-hat filter extending from 3000 Å to 9000 Å.

In *B*, *V*, *R*, and *I*, the light curves for all observer orientations reach a peak around 20–25 days after explosion (see Table 2)

[6] For convenience, the filter functions are shown in the upper panel of Figure 5.

Table 3
Δm_{15}—the Increase in Magnitude from Peak to 15 Days after Peak in *U*, *B*, *V*, *R*, and *I* Bands for Different Observer Inclination Angles

	U				*B*				*V*				*R*				*I*			
Model	25°[a]	45°	60°	85°	25°	45°	60°	85°	25°	45°	60°	85°	25°	45°	60°	85°	25°	45°	60°	85°
A1	0.4	1.0	1.0	0.8	0.7[b]				0.9				0.9				0.7	0.6	0.7	0.6
A0.1	0.6	1.0	1.1	1.0	1.1				1.0				1.0				0.6			
C1	0.9	0.7	0.9	0.9	0.7				0.9	0.8	0.8	0.8	0.9	0.9	0.9	0.7	0.7	0.6	0.6	0.6
C0.1	1.0				1.1	1.0	1.1	1.0	1.0	0.9	0.8	0.9	0.9	0.9	0.9	0.7	0.6	0.6	0.6	0.5
F1	1.0				0.6				0.6				0.6				0.4			
F0.1	1.2				1.0				0.7				0.6				0.4			

Notes.
[a] Values are quoted for four observer inclination angles (measured relative to the polar axis).
[b] One number for all columns implies no angle dependency.

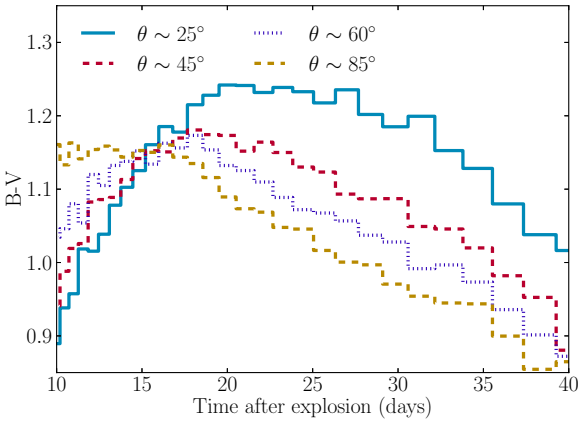

Figure 3. $B-V$ color evolution for model A1 for the different viewing angles. $\theta = 0°$ is the jet direction and $\theta = 90°$ is the equator. See the top panel of Figure 5 for the filter curves.
(A color version of this figure is available in the online journal.)

(∼7 days later than typical for SNe associated with GRBs, see Section 4) and then decline monotonically. In these bands, the time of peak depends only weakly on the observer orientation but tends to be earlier for inclinations close to the pole (small θ), particularly in the bluer bands. In *U* band, the influence of orientation is much stronger—the *U* light curve rises much more quickly and peaks around 10 days earlier for a polar compared to equatorial inclination. The widely used light curve decline rate parameter Δm_{15} (the increase in magnitude from peak to 15 days after peak) is similar for the asymmetric models and varies slightly with angles (see Table 3).

In general, the pre-maximum light curves are brighter for polar inclinations but around the peak the equatorial light curves become brighter. Since the angle dependence is strongest in the bluest bands, there are also significant differences in the color evolution for polar and equatorial lines of sight. This is illustrated in Figure 3, which shows the $B-V$ color evolution for model A1. If viewed close to the polar direction, the color becomes dramatically redder during the evolution toward maximum light. In contrast, the equatorial color evolution is much weaker, showing increasing blueward evolution starting a few days prior to maximum light. Similar orientation-dependent trends are predicted in our other asymmetric models. The scale is smaller in the more spherical models (in model C1 the difference between $B-V$ for polar and equatorial viewing angle at maximum light is 0.1 mag) and larger in corresponding models with reduced metallicity (e.g., model A0.1, where the difference is 0.45 mag; see Section 3.4).

The origin of the angle dependence in our light curves and colors can be largely traced to the asymmetric distribution of iron-group nuclei, particularly ^{56}Ni and its decay products (see Figure 1), and the evolution of the ionization state of the ejecta, which is shown in Figure 4. At early times, the effective photosphere is located at relatively high velocities. Since the ^{56}Ni distribution is most extended around the poles, it is there that the photosphere is first most directly heated, leading to initially stronger polar emission. The ionization state is generally high at early times (e.g., in the ^{56}Ni-rich regions, Co is dominated by Co III as seen in Figure 4[7]), such that this emission is fairly blue. As the ejecta expands, the opacity of the outer ejecta drops and the photosphere recedes deeper into the ejecta. Once radiation starts to escape from the inner ejecta, the larger projected area of the ^{56}Ni-rich region for equatorial inclinations generally favors brighter peak magnitudes for these orientations. At the same time, the line blanketing in the blue is stronger along the poles where metals synthesized in the explosion are present in the region around the photosphere. This leads to relatively red colors. This iron-group material is mostly singly and doubly ionized (upper panels of Figure 4) but it gradually recombines, causing the polar line blanketing to become even stronger with time in the rise to maximum light.

3.2. Si II Velocity and Correlation with Color

The Si II 6355 Å transition is an unmistakable absorption feature that is commonly seen in the red part of SN spectra. The asphericity of the Si-rich region (see Figure 1) gives rise to a significant angle dependence of the Si II 6355 Å absorption line velocity. This was previously reported by T07 and is confirmed in our study (see Figure 5, which shows the optical spectra computed for our models at *V*-band maximum light). To illustrate the origin of the angle dependence of the Si line, Figure 6 shows the Sobolev optical depth of the 6355 Å line at 15, 25, and 35 days for models A1, C1, and F1 and indicates the location of the region of last interaction for escaping *R*-band photons. At all epochs, the region in which the line is optically thick extends to significantly higher velocity along the polar than equatorial direction (in models A1 and C1). Therefore, the absorption extends to higher velocity in the spectrum when observed pole-on. Notice, however, that in most cases the region of last interaction for escaping *R*-band photons

[7] In Figure 4, we chose to show Co as an indicator for the typical ionization conditions for iron-group elements synthesized in the explosion. For the epochs shown in the plot, ^{56}Co is the most abundant iron-group isotope although we note that other iron-group elements (including Ti, Cr, and Ni) are still very important for line blocking in the blue.

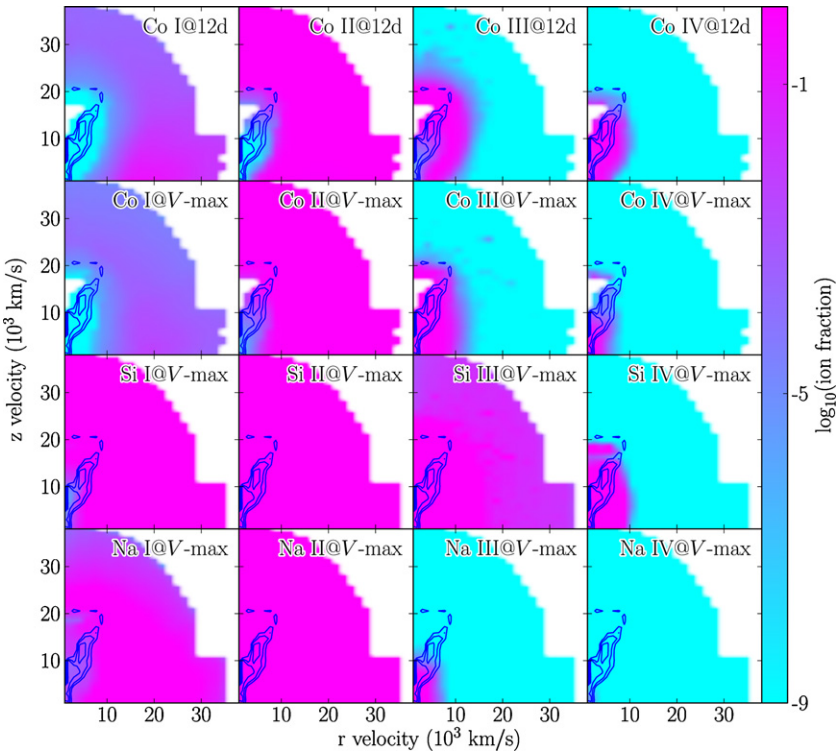

Figure 4. Ion fractions for model A1. From left to right the ions increase from I to IV, from top to bottom the ions are Co at 12 days (∼10 days before *V*-band maximum lights), and Co, Si, and Na at *V*-band maximum light (see Table 2 for details). The blue curves are contours of the ^{56}Ni mass fraction and correspond to 0.05, 0.07, and 0.09.

(A color version of this figure is available in the online journal.)

does extend outside the region in which the Si line is optically thick. Consequently, the Si line trough has usually been partially refilled such that the line core does not appear to be saturated.

The same trend appears across the spectrum and can clearly be seen in the Ca II triplet, especially on the blue side of the emission part. Higher velocities toward the equator are also seen in the blue (e.g., ∼4400 Å), although the overlapping of many Fe, Ti, and Co lines makes quantitative analysis more complicated in this region.

As discussed in Section 3.1, the SN colors at maximum light also show a systematic dependence on the observer orientation. Consequently, our simulations predict that the Si velocity and the color should be correlated for SNe described by the M02 models. This predicted correlation is shown in Figure 7. For all our aspherical models, we find that decreasing the inclination angle causes the peak $B-V$ color to become systematically redder while the Si II velocity becomes simultaneously higher. The range of variation depends on the degree of asphericity. Clearly, the spherically symmetric models show no variation with observer orientation, while in model A1 we find the $B-V$ color to differ by up to ∼0.16 mag and the range of Si II velocities ($\Delta v_{\rm Si\,II}$) to be ∼6300 km s^{-1}. Model C1 shows a similar correlation to that in model A1, except that the range of variation is smaller since the degree of asphericity is lower.

We find that this correlation between line velocity and color is present in the simulations from ∼18 days after explosion for as long as the Si line remains in the spectrum. However, it changes slightly at different epochs. For example, in model A1, the absolute Si velocities decrease after maximum light and the amplitude of the color variation with viewing angle becomes slightly smaller (see Figure 3). Nevertheless, the correlation persists and, for 18 days after explosion and all later epochs, is always in the same sense (redder colors are associated with higher line velocity).

3.3. Na I Absorption

One of the strongest features in our synthetic spectra is the Na I 5890 Å absorption line (see Figure 5). In general, we find this feature to have similar strength and angle dependency as reported by T07. The Na in the ejecta is predominantly in the unburned material. Its abundance is therefore governed by the Na mass fraction in the pre-explosion stellar model and is uniform in the outer ejecta (Figure 1). Due to the high optical depth of this ground state transition, only a small Na mass fraction is required to make the line strong, if the ionization state is sufficiently low to favor Na I. The angle dependence of the Na line is therefore not a consequence of the spatial distribution of the Na abundance, but of variations in the ionization state (see Figure 8). Particularly for early times, it is only in the relatively dense equatorial regions that the Na I population is sufficiently high that the line is very strong (see Figure 9). However, at later times sufficient recombination occurs that the line becomes significant for all orientations.

As noted by T07, the GRB related SN 1998bw did not show strong Na I absorption, which is consistent with the models for a pole-on viewing angle around maximum light. However, the Na I line remains a challenge for our models since the synthetic observables for equatorial orientations are expected to correspond to cases in which the jet axis is not close to our line of sight. Such off-axis explosions should produce a sub-population of SNe Ic. However, strong Na I is not typically observed for broad-lined core-collapse SNe. This may simply be a failing of the particular explosion models and/or ionization treatment adopted here. As discussed above, the formation of this feature

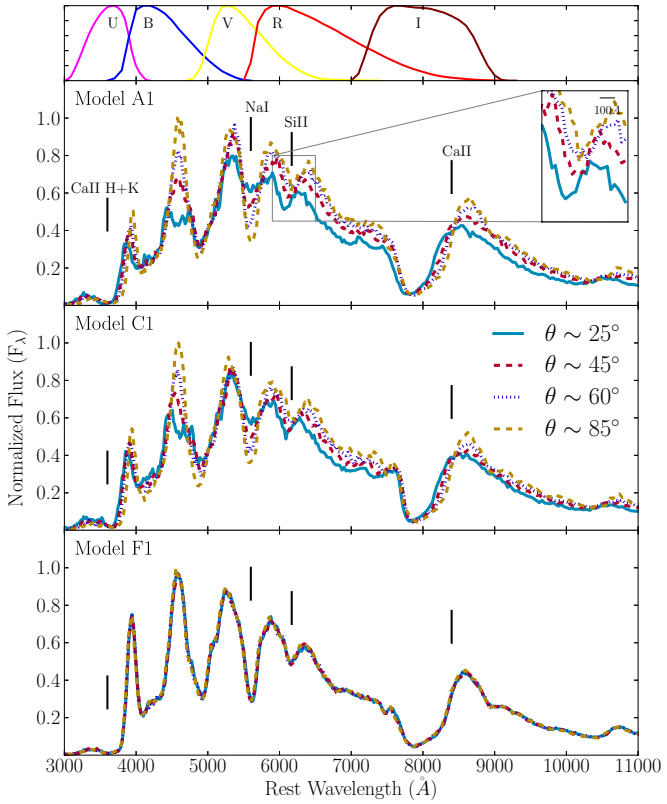

Figure 5. Synthetic spectra at *V*-band maximum (see Table 2 for details) light for models A1 (most asymmetric), C1 (intermediate symmetry), and F1 (spherically symmetric, upper, middle, and lower panels, respectively) for different viewing angles. The top panel shows the filter functions used to generate the light curves in Figure 2. $\theta = 0°$ is the jet direction and $\theta = 90°$ is the equator.

(A color version of this figure is available in the online journal.)

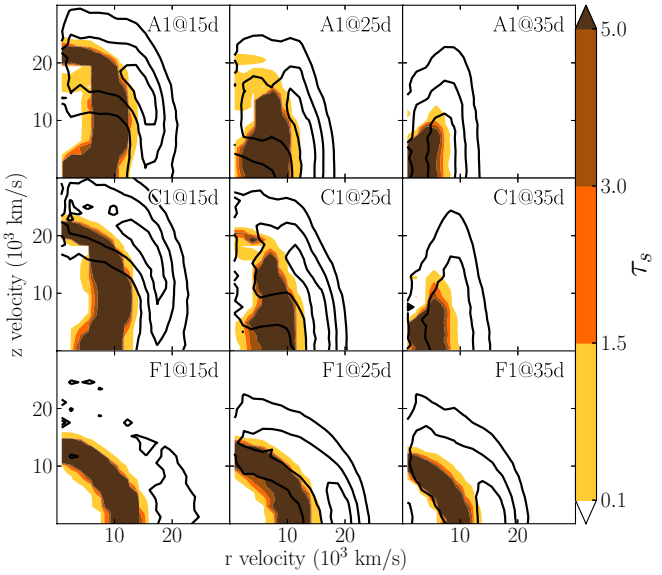

Figure 6. Sobolev optical depth (color coded) of the Si II 6355 Å line for models A1, C1, and F1 (from top to bottom) at times 15, 25, and 35 days after explosion (from left to right). The black contours indicate the area of last interaction of escaping *R*-band photons at that time (effective photosphere). The contours correspond to 0.2, 0.5, and 0.8 of the emissivity normalized to peak value.

(A color version of this figure is available in the online journal.)

is very sensitive to the degree of ionization in the outer ejecta and it could be suppressed if the ionization remained slightly higher. Increased ionization could be achieved in models with somewhat higher ^{56}Ni masses (as would be required to account for the brightness of, e.g., 1998bw; Maeda 2006).

3.4. Metallicity Dependence

Studies reveal a possible link between the metallicity of the SN environment and whether it will produce a GRB (Sollerman et al. 2005; Modjaz et al. 2006, 2008; Levesque et al. 2010). However, conclusive results are still limited by the small sample of spectroscopically confirmed GRB–SNe, only one of which has had sufficiently complete observations to be modeled in detail (2003dh; Mazzali et al. 2003; Matheson et al. 2003; Stanek et al. 2003; Šimon et al. 2004; Deng et al. 2005). Sollerman et al. (2005) observed three galaxies which were identified to host an SN with an associated GRB. Their results favor low-metallicity, sub-luminous galaxies in a phase of active star formation, which agrees with other studies of higher redshift GRBs (Le Floc'h et al. 2003). It is therefore important to consider how our synthetic observables are affected by a reduced progenitor metallicity, to confirm the robustness of our findings and identify potential observable signatures of progenitor metallicity in the SN itself.

Figure 10 shows spectra for our sub-solar metallicity model A0.1 and solar metallicity model A1 for the same epoch as shown for model A1 in Figure 5. The biggest difference is increased flux in the blue part of the spectrum for all orientations, a consequence of less line blocking from primordial heavy elements in the lower metallicity model. This persists for all epochs and results in light curves that are systematically brighter up to ∼35 days past explosion and reach peak earlier, in *B* and *U* for model A0.1 (Figure 11) compared to model A1. We draw similar conclusions when comparing the spherically symmetric models.

Since the metallicity affects the redder bands much less significantly, the increased blue flux from the sub-solar metallicity models influences the colors. The sub-solar models are always bluer and also show a wider variation of color with orientation. This makes the Si II–color correlation even stronger (and, consequently, more detectable), spanning a range of $\Delta(B - V) \sim 0.5$ around peak (see results for model A1 in Figure 7). The trend in the correlation with time is different to that found in model A1 with a plateau around peak and a beginning of decrease ∼35 days past explosion.

4. DISCUSSION AND CONCLUSION

We performed multi-dimensional radiative transfer calculations to compute light curves and spectra for two-dimensional models of SNe driven by bipolar outflows. Compared to previous studies, the main advantage of our work is the use of self-consistent opacities in a time-dependent calculation of the spectral evolution.

As expected for strongly asymmetric explosion models, we find that many observable properties depend on the orientation of the observer. During the rise phase, the synthetic light curves are brighter and the colors are bluer for an observer inclination close to the polar axis. However, at peak, the pole-on light curves are slightly fainter and redder than those seen from an equatorial orientation. This is a consequence of the concentration of ^{56}Ni along the polar direction in the explosion models. The time of maximum light also depends slightly on inclination and is reached a few days earlier for pole-on inclinations, in agreement with the findings by Maeda (2006).

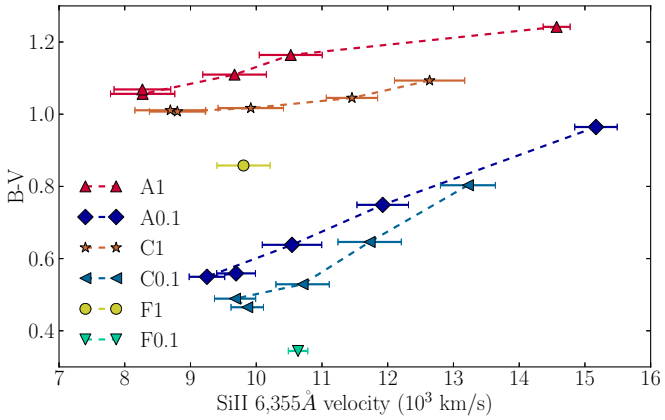

Figure 7. $B-V$ color vs. Si II velocity for all the models at V-band maximum light (see Table 2 for details). For the aspherical models (A1, A0.1, C1, and C0.1), the symbols represent data points at 25°, 45°, 60°, 72°, and 85° with decreasing Si velocity (from right to left). The horizontal error bars indicate the uncertainties associated with fitting the line velocity from our MC spectra. The lines connect the data points to guide the eye.

(A color version of this figure is available in the online journal.)

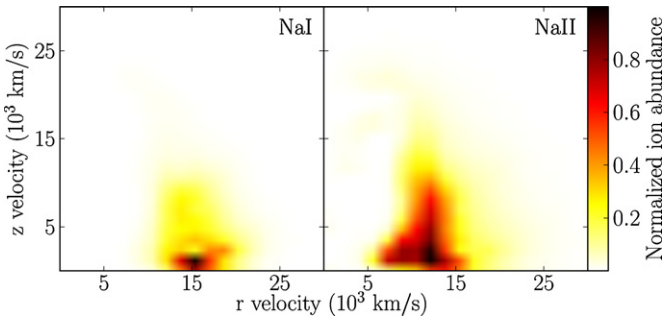

Figure 8. Na I (left) and Na II (right) density distribution for model A1 at V-band maximum light (see Table 2 for details). In both panels, the distributions are normalized to a maximum value of 1.0. The neutral Na is concentrated along the $\theta \sim 90°$ direction explaining the deep absorption observed from an equatorial orientation.

(A color version of this figure is available in the online journal.)

The color evolution of our sub-solar metallicity aspherical model A0.1 in the pole-on case shows similar trends to 1998bw: $B-V$ increases with time, although less quickly in our model than for 1998bw. We note, however, that 1998bw is systematically bluer at all times by 0.2–0.4 mag. In our models, we find low metallicity makes the peak $B-V$ color bluer and increases the steepness of the $B-V$ temporal color evolution around the peak, suggesting that even lower metallicity might be worthy of investigation for 1998bw. Comparing our off-axis color evolution to SN 2009bb, a BL-Ic SN without a GRB, we find similar results (i.e., with a slower color evolution and redder color in our model than those found by Pignata et al. 2011 for the SN).

Our asymmetric models predict that an on-axis orientation gives rise to a redder $B-V$ color at peak. This should be statistically testable if a large sample of potential jet-driven SNe Ic (including events observed both on- and off-axis) were identified. This could be most clearly done with a set of objects for which the ejecta mass and energy are similar. However, even for a sample with a range of explosion energies and masses, a mean trend in the ensemble averages might be detectable.

These orientation-dependent effects on the light curve mean that one would overestimate the ejected mass and ^{56}Ni (by on the order of tens of percent) if applying the widely used Arnett

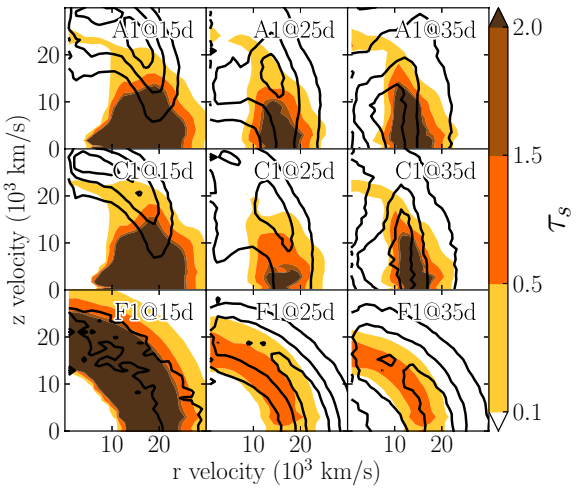

Figure 9. Sobolev optical depth (color coded) of the Na I 5890 Å line for models A1, C1, and F1 (from top to bottom) at times 15, 25, and 35 days after explosion (from left to right). The black contours indicate the area of last interaction of escaping V-band photons at that time (effective photosphere). The contours correspond to 0.2, 0.5, and 0.8 of the emissivity normalized to peak value.

(A color version of this figure is available in the online journal.)

relation (Arnett 1982) to the equatorially viewed light curve, and underestimate these parameters when viewing the SN pole-on.

Spectral features also depend on the viewing angle. As already noted by T07, the Si II line velocity at maximum light varies monotonically (within our MC uncertainties) with orientation, being fastest for pole-on inclinations. We find the Si II velocities along the poles to be comparable with those reported for SNe associated with GRBs such as 1998bw and 2003lw, while our off-axis velocities are comparable to BL-Ic SNe such as 1997ef and 2003bg (Corsi et al. 2011). Since our light curve properties also show a simple trend with viewing angle, this means we predict an Si II velocity–peak color ($B-V$) correlation. We found that this correlation is robust: it is predicted for solar and sub-solar models during a significant range of observable epochs and for a range in asphericities. Such a correlation should be statistically testable if a large sample of potential jet-driven SNe Ic (including events observed both on- and off-axis) were identified.

We examined the role of progenitor composition on the light curves and spectra by considering models appropriate for both solar and one-tenth solar metallicity. We showed that the metallicity strongly influences the blue part of the spectrum (the $B-V$ color is roughly 0.2–0.8 mag bluer for $Z = 0.1\ Z_\odot$ compared to $Z = 1\ Z_\odot$). Therefore, if GRB progenitors typically have low metallicity, we expect them to have measurably bluer colors than a typical stripped-envelope core-collapse SN with a more metal-rich progenitor. However, the metallicity does not qualitatively affect the trends of line-velocity and light curve color with orientation (indeed, we find that our velocity–color relationship is even stronger for $Z = 0.1\ Z_\odot$).

There are some shortcomings of our synthetic light curves and spectra in comparison to observations. Typically, our light curves reach peak at ~23 days, which is seven days later than typical for SNe associated with GRBs (Woosley & Bloom 2006) which could imply that the density distribution in the current models is somewhat inappropriate. Also, at most epochs in our models, we predict strong Na I absorption, which is not typical of SNe Ic. This may be attributed to the ionization state being too low in our current models. Further study and exploration of

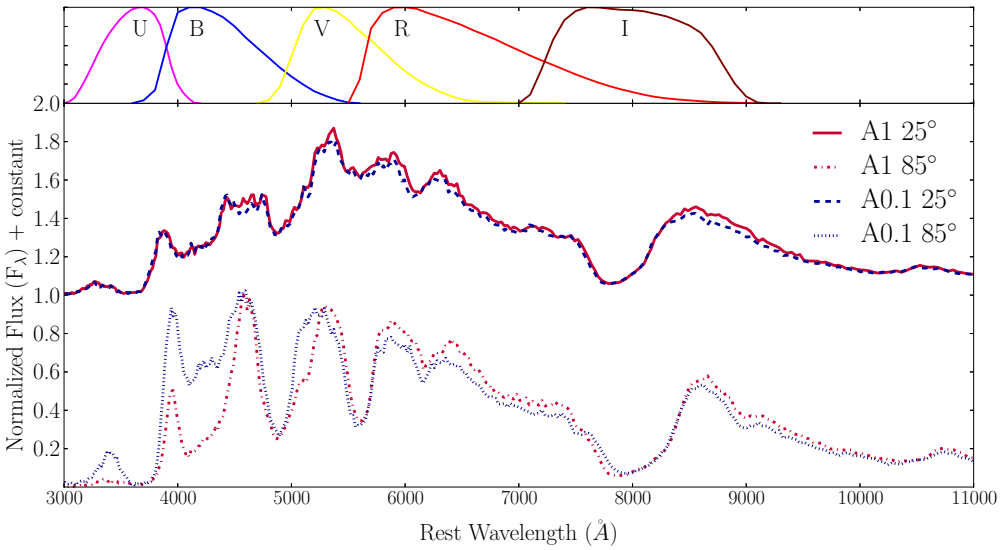

Figure 10. Synthetic spectra for models A1 and A0.1 at *V*-band maximum light for polar (∼25°) and equatorial (∼85°) viewing angles. The top panel shows the filter functions used to generate the light curves in Figures 2 and 11.

(A color version of this figure is available in the online journal.)

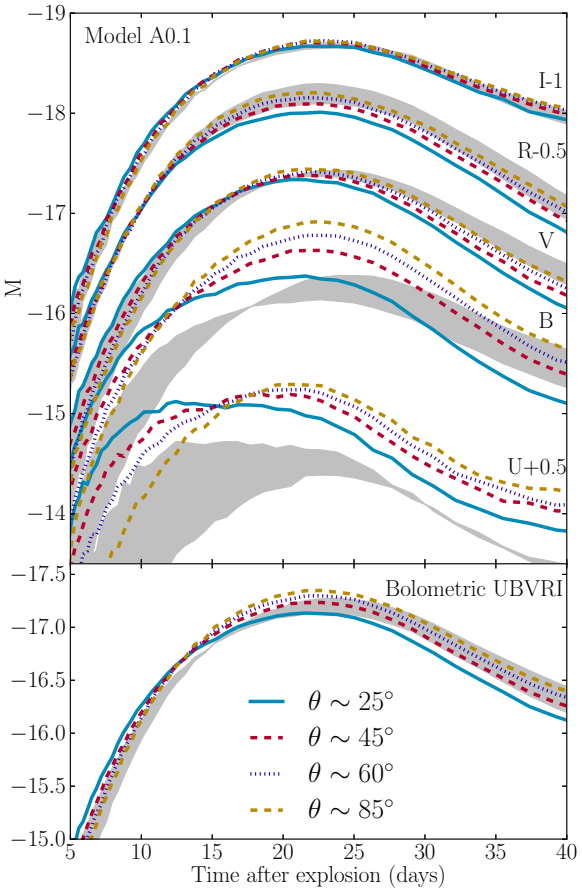

Figure 11. Light curves for model A0.1 for the different viewing angles. $\theta = 0°$ is the jet direction and $\theta = 90°$ is the equator. The shaded gray area spans the values for all angles for model A1 to allow comparison. See the top panel of Figure 5 for the filter curves.

(A color version of this figure is available in the online journal.)

different explosion model parameters is warranted to understand whether these issues can be resolved.

In this work we used the well-studied M02 models as a test case to compare our methods with previous results, and allow us to understand the limitations and strengths of our approach before applying them to a wider range of models. We have concentrated on only two of the parameters that are relevant to asymmetric Type Ic explosions: the degree of asphericity and the composition (i.e., metallicity). However, to fully explore this class of models and make quantitative comparisons to observed explosions, we will extend this work to span a range of masses and explosion energies. Having such a grid of synthetic spectra for models with different explosion parameters will help to quickly identify parameter ranges for newly observed GRB–SNe, on which more detailed modeling can be based.

S.R. and S.A.S. would like to thank the IPMU for their hospitality during their visit which resulted in this collaboration. B.P.S. acknowledges financial support through ARC Laureate Fellowship Grant FL0992131. S.R., S.A.S., and B.P.S. acknowledge the Centre for All-sky Astrophysics, Australian Research Council Centre of Excellence, funded by grant CE110001020. This research was undertaken with the assistance of resources provided at the NCI National Facility in Canberra, Australia, which is supported by the Australian Commonwealth Government, through the National Computational Merit Allocation and the ANU Partner Share Schemes supported by the Australian Government. This research is supported by the World Premier International Research Center Initiative (WPI Initiative), MEXT, Japan. K.M. acknowledges support by Grant-in-aid for Scientific Research (23740141). We thank the anonymous referee for their constructive comments.

REFERENCES

Anders, E., & Grevesse, N. 1989, Geochim. Cosmochim. Acta, 53, 197
Arnett, W. D. 1982, ApJ, 253, 785
Berger, E., Chornock, R., Holmes, T. R., et al. 2011, ApJ, 743, 204
Bessell, M., & Murphy, S. 2012, PASP, 124, 140
Bloom, J. S., Kulkarni, S. R., Djorgovski, S. G., et al. 1999, Nature, 401, 453
Bucciantini, N., Quataert, E., Metzger, B. D., et al. 2009, MNRAS, 396, 2038
Bufano, F., Pian, E., Sollerman, J., et al. 2012, ApJ, 753, 67
Campana, S., Mangano, V., Blustin, A. J., et al. 2006, Nature, 442, 1008
Cano, Z., Bersier, D., Guidorzi, C., et al. 2011, ApJ, 740, 41
Conselice, C. J., Vreeswijk, P. M., Fruchter, A. S., et al. 2005, ApJ, 633, 29
Corsi, A., Ofek, E. O., Frail, D. A., et al. 2011, ApJ, 741, 76

Deng, J., Tominaga, N., Mazzali, P. A., Maeda, K., & Nomoto, K. 2005, ApJ, 624, 898
Fryer, C. L., Mazzali, P. A., Prochaska, J., et al. 2007, PASP, 119, 1211
Galama, T. J., Vreeswijk, P. M., van Paradijs, J., et al. 1998, Nature, 395, 670
Greiner, J., Peimbert, M., Estaban, C., et al. 2003, GRB Coordinates Network, 2020, 1
Heger, A., Fryer, C. L., Woosley, S. E., Langer, N., & Hartmann, D. H. 2003, ApJ, 591, 288
Hjorth, J., Sollerman, J., Mller, P., et al. 2003, Nature, 423, 847
Iwamoto, K., Mazzali, P. A., Nomoto, K., et al. 1998, Nature, 395, 672
Kasen, D., Thomas, R. C., & Nugent, P. 2006, ApJ, 651, 366
Kromer, M., & Sim, S. A. 2009, MNRAS, 398, 1809
Kulkarni, S. R., Frail, D. A., Wieringa, M. H., et al. 1998, Nature, 395, 663
Kurucz, R., & Bell, B. 1995, Atomic Line Data, Kurucz CD-ROM No. 23, (Cambridge, MA: Smithsonian Astrophysical Observatory), 23
Le Floc'h, E., Duc, P.-A., Mirabel, I. F., et al. 2003, A&A, 400, 499
Levesque, E. M., Kewley, L. J., Berger, E., & Zahid, H. J. 2010, AJ, 140, 1557
Lindner, C. C., Milosavljević, M., Couch, S. M., & Kumar, P. 2010, ApJ, 713, 800
Lucy, L. B. 2002, A&A, 384, 725
Lucy, L. B. 2003, A&A, 403, 261
Lucy, L. B. 2005, A&A, 429, 19
MacFadyen, A. I., & Woosley, S. E. 1999, ApJ, 524, 262
Maeda, K. 2006, ApJ, 644, 385
Maeda, K., Kawabata, K., Mazzali, P. A., et al. 2008, Science, 319, 1220
Maeda, K., Mazzali, P. A., & Nomoto, K. 2006, ApJ, 645, 1331
Maeda, K., Nakamura, T., Nomoto, K., et al. 2002, ApJ, 565, 405
Matheson, T., Garnavich, P. M., Stanek, K. Z., et al. 2003, ApJ, 599, 394
Mazzali, P. A., Deng, J., Tominaga, N., et al. 2003, ApJ, 599, L95
Mészáros, P. 2006, Rep. Prog. Phys., 69, 2259
Meynet, G., Chiappini, C., Georgy, C., et al. 2009, in IAU Symp. 254, ed. J. Andersen, J. Bland-Hawthorn, & B. Nordström (Cambridge: Cambridge Univ. Press), 325
Modjaz, M., Kewley, L., Kirshner, R. P., et al. 2008, AJ, 135, 1136
Modjaz, M., Stanek, K. Z., Garnavich, P. M., et al. 2006, ApJ, 645, L21
Nomoto, K., Maeda, K., Mazzali, P. A., et al. 2004, in Stellar Collapse, ed. C. L. Fryer (Astrophysics and Space Science Library; Dordrecht: Kluwer), 277
Nomoto, K., Tominaga, N., Umeda, H., Kobayashi, C., & Maeda, K. 2006, Nucl. Phys. A, 777, 424
Olivares, E. F., Greiner, J., Schady, P., et al. 2012, A&A, 539, A76
Pian, E., Mazzali, P. A., Masetti, N., et al. 2006, Nature, 442, 1011
Pignata, G., Stritzinger, M., Soderberg, A., et al. 2011, ApJ, 728, 14
Price, P. A., Fox, D. W., Kulkarni, S. R., et al. 2003, Nature, 423, 844
Proga, D., MacFadyen, A. I., Armitage, P. J., & Begelman, M. C. 2003, ApJ, 599, L5
Sawai, H., Kotake, K., & Yamada, S. 2005, ApJ, 631, 446
Sim, S. A. 2007, MNRAS, 375, 154
Soderberg, A. M., Chakraborti, S., Pignata, G., et al. 2010, Nature, 463, 513
Soderberg, A. M., Nakar, E., Berger, E., & Kulkarni, S. R. 2006, ApJ, 638, 930
Sollerman, J., Östlin, G., Fynbo, J. P. U., et al. 2005, New Astron., 11, 103
Stanek, K. Z., Matheson, T., Garnavich, P. M., et al. 2003, ApJ, 591, L17
Šimon, V., Hudec, R., & Pizzichini, G. 2004, A&A, 427, 901
Tanaka, M., Maeda, K., Mazzali, P. A., & Nomoto, K. 2007, ApJ, 668, L19
Taubenberger, S., Valenti, S., Benetti, S., et al. 2009, MNRAS, 397, 677
Woosley, S. E. 1993, ApJ, 405, 273
Woosley, S. E., & Bloom, J. S. 2006, ARA&A, 44, 507
Woosley, S. E., Eastman, R. G., & Schmidt, B. P. 1999, ApJ, 516, 788
Woosley, S. E., & Heger, A. 2006, ApJ, 637, 914
Woosley, S. E., & Zhang, W. 2007, Phil. Trans. R. Soc. A, 365, 1129
Yamazaki, R., Ioka, K., & Nakamura, T. 2004, in AIP Conf. Ser. 727, Gamma-Ray Bursts: 30 Years of Discovery, ed. E. Fenimore & M. Galassi (Melville, NY: AIP), 115
Yoon, S.-C., & Langer, N. 2005, A&A, 443, 643